International Journal of Plasticity 147 (2021) 103123

Contents lists available at ScienceDirect

International Journal of Plasticity

journal homepage: www.elsevier.com/locate/ijplas

Void growth based inter-granular ductile fracture in strain gradient polycrystalline plasticity

T. Yalçinkaya [a,*], İ.T. Tandoğan [a], İ. Özdemir [b]

[a] Department of Aerospace Engineering, Middle East Technical University, Ankara 06800, Turkey
[b] İzmir Institute of Technology, Faculty of Engineering, Department of Civil Engineering, 35430 Urla, İzmir, Turkey

ARTICLE INFO

Keywords:
Strain gradient plasticity
Size effect
Grain boundary
Crystal plasticity
Ductile fracture

ABSTRACT

The precipitation hardened, high strength aerospace alloys (e.g. Al 7000 alloy series) suffer from loss of fracture toughness due to the heat treatment leading to intergranular ductile fracture. Depending on the quenching and aging processes, large precipitates at the grain boundaries with wide precipitate free zones might develop. Therefore the grain boundaries constitute a potential location for micro void formation and evolution under the effect of external loads. This is a common problem of such materials where there is considerable ductile intergranular fracture, which is normally attributed to the embrittlement effects of the environment in other type of alloys. In this context, for the modeling of such a degradation process, the current paper develops a physics based intergranular cracking model of polycrystalline materials where a strain gradient crystal plasticity model is combined with cohesive zone elements whose traction separation relation is based on the evolution of micro-voids at the grain boundaries. The framework successfully predicts the intergranular crack formation and propagation, taking into account different microstructural features, such as porosity, pore shape, grain orientation distribution, and grain boundary conditions.

1. Introduction

The high strength aerospace alloys, e.g. 7xxx aluminum alloy series, used in the production of structural frames and components, are hardened through an appropriate heat treatment leading to fine scale precipitation (see e.g. Deschamps et al., 1999). The failure mechanisms of these materials are completely dependent on the microstructure evolving due to heat treatment procedure followed in the manufacturing process. Depending on the quenching rate and aging treatment the microstructure could lead to transgranular or intergranular ductile cracking dominated fracture phenomenon (see e.g. Ludtka and Laughlin, 1982; Vasudevan and Doherty, 1987; Kuramoto et al., 1996; Dumont et al., 2003; Pardoen et al., 2003). The main heterogeneities affecting the failure mechanism are the grain boundaries, whose state with precipitates and chemical composition lead to initiation of the cracks. The most severe and well studied case of such situation is when the grain boundary is embrittled because of the chemical segregation (see e.g. Knight et al., 2010; Rao et al., 2016; Li et al., 2020; Singh and Pal, 2020; Isfandbod and Martínez-Pañeda, 2021; Liang et al., 2021). Another important failure mechanism in these materials is encountered when the grain boundaries are weakened by a specific state of precipitation around them, but they remain strong enough that the failure in the vicinity of the grain boundaries is ductile. This mechanism is known as intergranular ductile fracture that is very well known in aerospace aluminum alloys and the subject of the current work. Even though such fracture mechanism is common at high temperatures, it is often observed in these materials at room temperature as well.

* Corresponding author.
E-mail address: yalcinka@metu.edu.tr (T. Yalçinkaya).

https://doi.org/10.1016/j.ijplas.2021.103123
Received 24 June 2021; Received in revised form 6 September 2021
Available online 2 October 2021

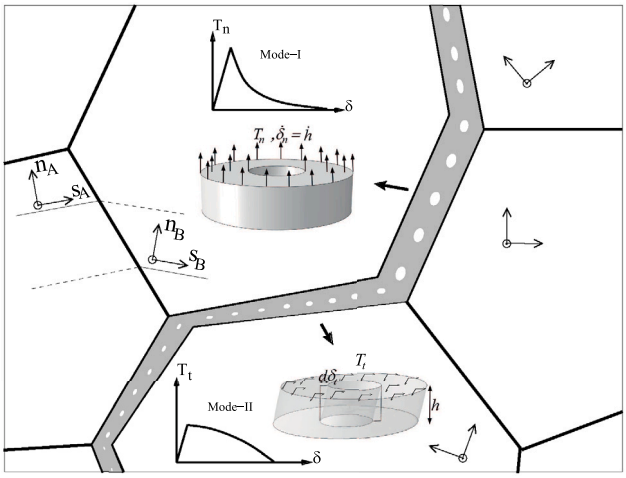

Fig. 1. The physical illustration of the intergranular ductile cracking mechanisms.

While after a fast quench there is no precipitation observed in these materials, they appear during a subsequent aging treatment around the grain boundaries, which are rather small in over-aged condition. After a slower quench, the precipitates are present largely at the grain boundaries which get bigger with slower quench rates (see the observations in e.g. Dumont et al., 2003). These precipitates are accompanied with the precipitate free zones (PFZ) around the grain boundaries (see e.g. Unwin et al., 1969; Pardoen et al., 2003). The PFZ is naturally rather soft and deforms first plastically. In this situation the elastic or harder grains impose a strong constraint on the PFZ involving large stress triaxiality. It is very well known now that the higher triaxiality values give larger void growth rate (see e.g. Rousselier, 2021; Bronkhorst et al., 2021; Frodal et al., 2021) leading to rapid coalescence of voids and the initiation of related intergranular cracking. When in some circumstances the stress in the grains reaches the yield stress before the onset of coalescence in the PFZ; the stress triaxiality then drops in the PFZ then the transgranular fracture mechanism might occur as well. The competition between these two failure mechanisms was studied in a very simplified definition of microstructure with various parameters that gave certain conclusions about the loading and the microstructure on the initiation of the cracks. However a realistic model with physics based plasticity and fracture mechanics models considering the effect of different microstructural parameters of the intergranular failure behavior of these materials have never been addressed before and it is the main objective of the current work. There have been some recent studies focusing on the ductile failure in the grain boundaries (see e.g. Benedetti and Aliabadi, 2013; Simonovski and Cizelj, 2015; Molkeri et al., 2019; Bond and Zikry, 2018; Yalcinkaya et al., 2019; Liu et al., 2021; Khadyko et al., 2021) using phenomenological or crystal plasticity approaches. A micromechanical description of void growth mechanism leading to failure at the grain boundaries and the non-local physical description of plasticity where the orientation mismatch leads to traction increase at the grain boundaries has never been addressed before. Therefore the current work makes a unique contribution to the literature by combining the underlying physical mechanisms of both plasticity and fracture in the ductile failure of grain boundaries in polycrystalline materials (see the physical illustration in Fig. 1).

In this context, the framework developed here, for the modeling of ductile intergranular fracture, combines a strain gradient crystal plasticity model (see e.g. Yalçinkaya et al., 2012, 2018) for bulk plasticity behavior in the grains with a micromechanics based cohesive zone model at the grain boundaries. Due to the higher-order nature of the crystal plasticity model, a mixed finite element formulation is used to discretize the problem in which both displacements and plastic slips are considered as primary variables. Therefore the boundary conditions could be defined in terms of both variables. Due to the orientation mismatch between the randomly oriented grains, stress concentration and increase in the normal and tangential traction occurs at the grain boundaries, which lead to the normal and tangential separation of the grain boundaries. The relation between the traction and separation is obtained by considering the evolution of representative volume elements where pores are idealized as cylinders. Upper bound theorem is applied, and the relations for both mode-I and mode-II are obtained in terms of physical parameters describing the evolution of micro voids. The physical picture of the modeling strategy is depicted in Fig. 1. The obtained micromechanics based cohesive relations are used in previously developed potential based cohesive zone elements (see e.g. Park et al., 2009; Cerrone et al., 2014) in a mixed mode environment which are inserted between the grains that are generated in three dimensions through Voronoi tesselation. This is the first attempt in the literature where two physics based plasticity and fracture frameworks are combined for intergranular ductile crack initiation and propagation in three dimensional micron sized specimens. Qualitative conclusions are obtained from the numerical analysis of micron sized specimens. Therefore, the model parameters are not fitted to a certain material, yet the analysis gives important conclusions on this type of degradation mechanism.

The paper is organized as follows. First, in Section 2, the formulations of both strain gradient crystal plasticity and the micromechanics based traction separation relations for cohesive zone elements are discussed. Then in Section 3, the numerical examples are presented where different aspects of the model are illustrated in polycrystalline specimens. Finally, the work is summarized and concluding remarks are given in Section 4.

2. Modeling framework

For the modeling of intergranular ductile fracture observed in certain high strength aerospace alloys, two models are combined here. To simulate bulk grain behavior a rate dependent strain gradient crystal plasticity model is used. The model and the governing equations are briefly discussed in the following. For the simulations of crack initiation and propagation between the grains, physically motivated traction-separation laws are developed. Traction-separation equations are obtained separately for mode-I and mode-II loading to be used in cohesive zone elements. For a perfectly plastic material the upper-bound theorem is employed, and the traction-separation equations are obtained in terms of morphological parameters of the deforming microstructure.

2.1. Rate dependent strain gradient crystal plasticity

Strain gradient crystal plasticity has been a promising tool to address the mechanical response of micron sized components during manufacturing (micro-forming) and in service. There are a number of strain gradient crystal plasticity theories/models which may differ in conjugate pairs used in their formulation and the primary variable used to describe size effect, e.g. gradient of dislocation densities (Gurtin, 2002; Evers et al., 2004; Yefimov et al., 2004) or gradient of slips (Yalçinkaya et al., 2012). These models are in fact closely related and unified treatments are presented in Kuroda and Tvergaard (2006) and Kuroda and Tvergaard (2008). In this paper, a rate dependent strain gradient crystal plasticity model is implemented in a three dimensional finite element framework for the prediction of anisotropic and size dependent plasticity behavior at grain scale to be used together with intergranular cohesive zone elements. While originally developed as a non-convex model for the modeling of deformation patterning in single crystals (see e.g. Yalçinkaya et al., 2012; Klusemann and Yalcinkaya, 2013; Klusemann et al., 2013), the size dependent nonlocal treatment of metallic materials is conducted with the convex counter-part of the model here. The model is implemented as an Abaqus user element subroutine (see Yalcinkaya, 2019 for the thermodynamics and finite element implementation details of the model). Note that only governing equations and important variables are shown here. Please refer to the presented references for the details.

Strain is decomposed into elastic and plastic parts additively in the small strain context. The slip law, which governs the plastic slip evolution is obtained from the thermodynamics principals as,

$$\dot{\gamma}^\alpha = \dot{\gamma}_0^\alpha (|\tau^\alpha + \nabla \cdot \boldsymbol{\xi}^\alpha| / s^\alpha)^{\frac{1}{m}} \operatorname{sign}(\tau^\alpha + \nabla \cdot \boldsymbol{\xi}^\alpha) \tag{1}$$

where $\tau^\alpha = \boldsymbol{\sigma} : \boldsymbol{P}^\alpha$ is the resolved Schmid stress on the slip systems with $\boldsymbol{P}^\alpha = \frac{1}{2}(\boldsymbol{s}^\alpha \otimes \boldsymbol{n}^\alpha + \boldsymbol{n}^\alpha \otimes \boldsymbol{s}^\alpha)$, the symmetrized Schmid tensor, where $\boldsymbol{s}^\alpha$ and $\boldsymbol{n}^\alpha$ are the unit slip direction vector and unit normal vector on slip system α, respectively. In here the influence of both elastic and nonlocal free energies are included directly in the evolution of plastic slip through the stress $\boldsymbol{\sigma} = d\psi_e / d\boldsymbol{\varepsilon}^e$ projected on the slip systems and the microstress vector $\boldsymbol{\xi}^\alpha = \partial \psi_{\nabla_\gamma} / \partial \nabla_{\gamma^\alpha}$ bringing the plastic slip gradients into the plasticity formulation. $A = ER^2/(16(1-\nu^2))$ is a scalar term including internal length scale parameter R which describes the radius of the dislocation domain contributing to the internal stress field, and it is linked to the average grain size here. Quadratic forms for the free energy terms are used; $\psi_e = \frac{1}{2}\boldsymbol{\varepsilon}^e : {}^4\boldsymbol{C} : \boldsymbol{\varepsilon}^e$ and $\psi_{\nabla\gamma} = \sum_\alpha \frac{1}{2} A \boldsymbol{\nabla}\gamma^\alpha \cdot \boldsymbol{\nabla}\gamma^\alpha$. The microscopic traction (associated with $\boldsymbol{\xi}$) on the outer boundaries of the specimen is defined in terms of scalar microscopic traction χ^α that satisfies,

$$\chi^\alpha = \boldsymbol{\xi} \cdot \bar{n} \tag{2}$$

whereas the interfacial tractions λ_A^α and λ_B^α are defined along the grain boundaries and fulfill,

$$\lambda_A^\alpha = \boldsymbol{\xi} \cdot N^A \tag{3}$$

$$\lambda_B^\alpha = \boldsymbol{\xi} \cdot N^B. \tag{4}$$

Please see Fig. 2 for the definition of $\bar{n}$, N^A and N^B. Due to intergranular cohesive fracture, in addition to essential and natural boundary conditions, traction continuity across the crack surfaces, i.e. grain boundaries, expressed in terms of traction vectors $\mathbf{t}_c^A$ and $\mathbf{t}_c^B$,

$$\mathbf{t}_{cz} = \mathbf{t}_c^B = -\mathbf{t}_c^A \text{ with } \mathbf{t}_c^A = \boldsymbol{\sigma}\,\mathbf{N}_A \text{ and } \mathbf{t}_c^B = \boldsymbol{\sigma}\,\mathbf{N}_B \tag{5}$$

has to be satisfied. Contrary to local crystal plasticity models where the displacements are considered to be the only degree of freedoms, in the current nonlocal strain gradient crystal plasticity framework both the displacement $\boldsymbol{u}$ and the plastic slips γ^α are taken as primary variables. This results in a fully coupled finite element solution algorithm for the solution of initial boundary value problem. The unknown fields are obtained by solving simultaneously:

$$\begin{aligned} \boldsymbol{\nabla} \cdot \boldsymbol{\sigma} &= \mathbf{0} \\ \dot{\gamma}^\alpha - \dot{\gamma}_0^\alpha \left[\frac{|\tau^\alpha + \nabla \cdot \xi^\alpha|}{s^\alpha} \right]^{1/m} \operatorname{sign}((\tau^\alpha + \nabla \cdot \xi^\alpha)) &= 0 \end{aligned} \tag{6}$$

where, the first line represents the linear momentum balance, the second one is the slip evolution equation with constant slip resistance without slip-level hardening. Then, the strong form of the governing equations is converted to weak form and linearized with respect to variation of primary variables. As compared to the explicit forms given in Özdemir and Yalcinkaya (2019), the weak form of the linear momentum balance is extended by δW_{cz} such that,

$$\delta W_{int} + \delta W_{cz} = \delta W_{ext} \quad \text{where} \quad \delta W_{cz} = \int_{S_{GB}} \mathbf{t}_{cz} \cdot \delta[\![\mathbf{u}]\!]\, dS \tag{7}$$

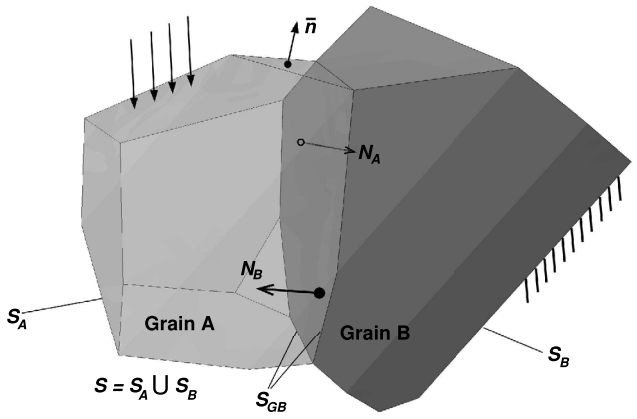

Fig. 2. The grain boundary representation in a two-grain body.

where $[\![\mathbf{u}]\!]$ is the displacement jump across the grain boundary, i.e. $[\![\mathbf{u}]\!] = \mathbf{u}_B - \mathbf{u}_A$ and $\mathbf{t}_{cz}$ is the cohesive traction vector. In the implementation phase, the displacement jump and cohesive traction are decomposed into normal and tangential components with respect to a local coordinate system, see Park et al. (2009). The specific form of the components of $\mathbf{t}_{cz}$ is going to be elaborated in the next section. The classical Galerkin formulation for the finite element solution is employed. The procedure results in a system of linear equations which are written in the matrix format,

$$\begin{bmatrix} \underline{K}^{uu} & \underline{K}^{u\gamma} \\ \underline{K}^{\gamma u} & \underline{K}^{\gamma\gamma} \end{bmatrix} \begin{bmatrix} \Delta\underline{u} \\ \Delta\underline{\gamma}^{\alpha} \end{bmatrix} = \begin{bmatrix} -\underline{R}^{u} + \underline{R}^{ext}_{u} \\ -\underline{R}^{\gamma} + \underline{R}^{ext}_{\gamma} \end{bmatrix} \tag{8}$$

where $\underline{K}^{uu}, \underline{K}^{u\gamma}, \underline{K}^{\gamma u}$ and $\underline{K}^{\gamma\gamma}$ represent the global tangent matrices while $\underline{R}^{u}$ and $\underline{R}^{\gamma}$ are the global residual columns. The contributions $\underline{R}^{ext}_{u}$ and $\underline{R}^{ext}_{\gamma}$ originate from the boundary terms.

As mentioned previously the global degrees of freedom in this framework are the displacement and the plastic slips, in terms of which the boundary conditions are defined. There are two types of boundary conditions that could be used at the grain boundaries for plasticity during polycrystal simulations. By setting

$$\lambda^{\alpha}_{A} = 0 \text{ and } \lambda^{\alpha}_{B} = 0 \tag{9}$$

soft boundary conditions are imposed such that the slips reaching to the grain boundary do not 'feel' the existence of the neighboring grain and/or resistance of the grain boundary. Obviously, in case of soft boundary condition, grain boundaries are traction free and in the relevant literature also called as micro-free boundary conditions. On the opposite end of the spectrum, hard boundary conditions lie which are achieved by setting

$$\gamma^{\alpha} = 0 \text{ for } \alpha = 1, n_s \tag{10}$$

where n_s is the number of slip systems considered. This type of boundary condition leads to the development of a boundary layer in terms of plastic slip and the related stress concentrations at the grain boundaries. Apart from these two boundary condition types, in the polycrystal simulations, continuous slip across the grain boundaries is also considered which can be stated as,

$$\gamma^{\alpha}|_{A} = \gamma^{\alpha}|_{B} \text{ on } S_{GB} \text{ for } \alpha = 1, n_s \tag{11}$$

and imposed by means of equality constraints during the numerical solution phase. In fact modeling of dislocation (slip)-grain boundary interaction is an active research problem on its own, (see Özdemir and Yalçinkaya, 2014; Yalçinkaya et al., 2021).

2.2. Cohesive zone modeling

A micromechanics based cohesive zone formulation is used for the modeling of ductile intergranular cracking. The main relations for the mode-I, mode-II and mixed-mode fracture are summarized in the following. Initial attempts of developing the cohesive zone relations have been addressed previously in proceedings by the authors (see e.g. Yalçinkaya and Cocks, 2016; Yalçinkaya et al., 2019), and the detailed derivation and implementation is presented in Tandoğan (2020). However, a complete micromechanical analysis has never been conducted before in polycrystalline plasticity.

2.2.1. Traction separation relation for mode-I loading

An array of cylindrical volumes, each with a cylindrical hole in the middle, are considered in a plane. Each cylinder has diameter $2l$, height h, and the hole represents an idealized pore with a radius of a (Fig. 3(a)). A single cylinder is taken as representative volume element and it is subjected to following boundary conditions (Fig. 3(b)),

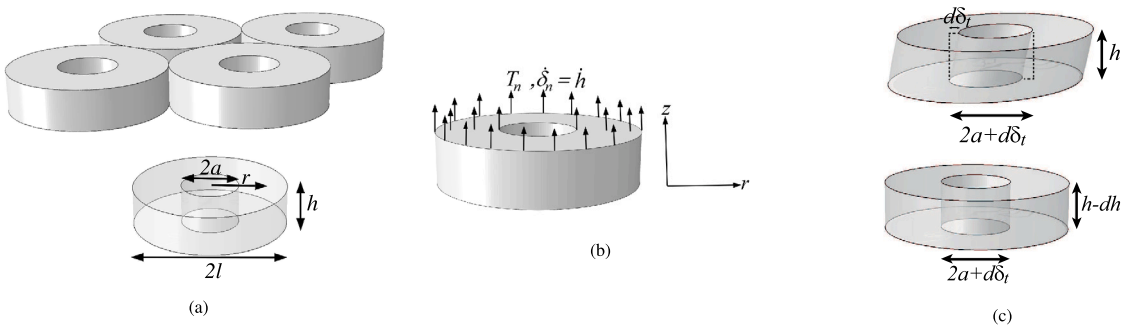

Fig. 3. Idealization of pores within a plane as cylinders (a), the response to normal traction (b) and geometry change of the cylindrical RVEs under shear deformation (c).

– $\delta_n = 0$ at $z = 0$, longitudinal displacement, δ_n, is fixed at the bottom surface of RVE.
– $u = 0$ at $r = l$, radial displacement, u, at outer lateral surface is zero, i.e. in plane macroscopic strain is zero.
– δ_n at $z = h$, uniform displacement is applied at the top surface of RVE.

For mode-I loading, RVE is displaced by δ_n in z direction. Since it is constrained, rate of displacement in normal direction is $\dot{\delta}_n = \dot{h}$. In order to obtain a relation between the normal traction and the displacement, upper bound theorem is employed here, which states that work done by the limit load is smaller or equal to the integral of energy dissipation of the effective strain rate at yield stress (12),

$$\pi l^2 T_n \dot{\delta}_n \leq \int_a^l \dot{\varepsilon_e} \sigma_y 2\pi r h dr \tag{12}$$

where T_n is normal traction, σ_y is the yield stress of matrix material, and $\dot{\varepsilon_e}$ is the effective strain rate. Here, displacement δ_n is applied uniformly with the goal to determine norm average stress. Therefore, T_n in Eq. (12) is the equivalent macroscopic traction acting on whole area, πl^2. If a perfectly plastic material is assumed, incompressibility condition in polar coordinates gives $\dot{\varepsilon_r} + \dot{\varepsilon_\theta} + \dot{\varepsilon_z} = 0$. Using small strain–displacement relations $\dot{\varepsilon_z} = \dot{h}/h$, $\dot{\varepsilon_\theta} = \dot{u}/r$, $\dot{\varepsilon_r} = \dot{u}/dr$ and the boundary conditions with the effective strain rate definition leads to (13),

$$T_n \leq \sigma_y \int_f^1 \sqrt{1 + \left(\frac{1}{3v^2}\right)} dv \quad \text{where} \quad v = r^2/l^2, \quad \text{and} \quad f = a^2/l^2 \tag{13}$$

with f being the area fraction of pores. Minkowski inequality (see Hardy et al., 1978) can be used to approximate the integral in (13), resulting in (14), i.e. traction as a function of pore fraction, f,

$$T_n \approx \sigma_y \left[(1-f)^2 + \left(\frac{1}{\sqrt{3}} ln \frac{1}{f} \right)^2 \right]^{\frac{1}{2}}. \tag{14}$$

Thus, the evolution relation for f is required for the calculation of traction. Since the matrix is incompressible, the conservation of volume can be used to obtain $df = (dh/h)(1-f)$. Evolution of h is directly given by boundary condition, $dh = d\delta_n$. Taking the integral and substituting f to (14) gives the mode-I traction-separation law (15) for given initial pore fraction, f_0, and initial pore height, h_0 (see Appendix).

$$T_n = \sigma_y \left[\left(\frac{h_0(1-f_0)}{(\delta_n + h_0)} \right)^2 + \left(\frac{1}{\sqrt{3}} ln \left(\frac{(\delta_n + h_0)}{(\delta_n + h_0 f_0)} \right) \right)^2 \right]^{\frac{1}{2}}. \tag{15}$$

2.2.2. Traction separation relation for mode-II loading

For mode-II, RVE is loaded in the radial direction. Shear loading elongates the pores in the shear direction and causes them to be more like a crack (Fleck and Hutchinson, 1986), which is not fully replicating the physical pore but is a reasonable approximation. The new shape is approximated as shown in Fig. 3. Upper bound theorem for mode-II loading gives (16),

$$\pi l^2 T_t \dot{\delta}_t \leq \int_a^l \dot{\varepsilon}_e \sigma_y 2\pi r h dr \tag{16}$$

where T_t is apparent average tangential traction. For pure mode-II effective strain rate can be written as, $\dot{\varepsilon}_e = (\dot{\gamma}^2/3)^{1/2}$ where $\dot{\gamma} = \dot{\delta}_t/h$. Substituting, applying the change of variables given in (13), then taking the integral results in (17) (see Appendix).

$$T_t \leq \frac{\sigma_y}{\sqrt{3}}(1-f). \tag{17}$$

The evolution of pore fraction is required for this case as well. From the definition of pore fraction, $f = a^2/l^2$ it reads $df = 2\sqrt{f}(d\delta_t/l)$. Assuming the volume of RVE is preserved under shear deformation, we get $dh = (d\delta_t/a)h$. Taking the integral of df and substituting to (17), results in mode-II traction-separation law (18) in terms of initial pore fraction, f_0, and pore spacing l,

$$T_t = \frac{\sigma_y}{\sqrt{3}}\left[1 - \left(\sqrt{f_0} + \frac{\delta_t}{l}\right)^2\right]. \tag{18}$$

2.2.3. Traction separation relation for mixed-mode loading

For mixed-mode it is assumed that mode-I and mode-II loadings occur simultaneously. Thus, when upper bound theorem is applied for mixed-mode with change of variables in (13) we get,

$$T_n\dot{\delta}_n + T_t\dot{\delta}_t \le \sigma_y \int_f^1 \sqrt{\dot{\delta}_n^2\left(1 + 1/(3v^2)\right) + \dot{\delta}_t^2/3}\,dv. \tag{19}$$

Applying Minkowski inequality to (19) and then minimizing right hand side of the inequality results in a yield function description (20). Superposing, for combined normal and shear deformation we get evolution Eqs. (21) for mixed-mode.

$$g = \left[\frac{T_n^2}{(1-f)^2 + \left((1/\sqrt{3})\,ln(1/f)\right)^2} + \frac{3T_t^2}{(1-f)^2}\right]^{\frac{1}{2}} - \sigma_y = \overline{\sigma} - \sigma_y \tag{20}$$

$$\begin{aligned} df &= d\delta_n(1-f)/h + d\delta_t 2\sqrt{f}/l \\ dh &= d\delta_n - d\delta_t h/a \end{aligned} \tag{21}$$

Eqs. (20) and (21) represent a system of nonlinear equations that should be satisfied under mixed-mode loading. Thus, unlike pure mode-I/II, obtaining tractions for given separations is not straightforward due to the yield type formulation. It is possible to employ an iterative numerical integration scheme for coupled elastoplastic and damage equations (Benallal et al., 1988), which is detailed in a recent MSc thesis (see Tandoğan, 2020). Even though the performance of such a incremental plasticity type of traction-separation update has been shown successfully in classical macroscopic fracture problems, a simpler approach is followed here due to numerical efficiency. Therefore, due to practicality and reproducibility the following alternative approach is considered in the current study.

2.2.4. Intrinsic/extrinsic TSL conversion

The traction-separation laws obtained for mode-I (15) and mode-II (18) are extrinsic TSLs, meaning traction starts from a finite value and then decreases. These types of TSLs require cohesive elements to be inserted during simulation when a fracture criterion is met. Hence, they are tedious to implement in commercial FE programs because mesh manipulation is required during analysis. On the other hand, in intrinsic laws, traction starts from zero and increases to a maximum value before decreasing again. This allows pre-insertion of cohesive elements, and significantly reduces implementation cost. Therefore, obtained TSLs are converted to intrinsic type by adding a linear elastic part. The slope of the elastic part is defined as, $E_n = T_{n,max}/\delta_{n,cr}$ and $E_t = T_{t,max}/\delta_{t,cr}$, where, $\delta_{n,cr}$ and $\delta_{t,cr}$ are the separations where the maximum traction is reached or softening starts. In the simulations, $\delta_{n,cr}$ and $\delta_{t,cr}$ are calculated for given slopes E_n and E_t. While they are easier to implement, a disadvantage of intrinsic TSLs is the artificial compliance problem, where the elastic region of TSL causes a reduction in the macroscopic stiffness response of the material. Therefore, in the following numerical simulations, elastic slope of TSL is chosen as high as possible, which also makes intrinsic TSL quite similar to extrinsic TSL.

The traction-separation relations obtained previously, (15) and (18), are physically motivated by pore growth. Note that these models are a simplification of what is really happening in the fracture process zone, but they capture the essential physics. These relations depend on f_0, initial pore fraction, h_0, initial pore height, l, mean spacing of pores, and σ_y, yield stress. Pores can obtain an elliptical shape during growth, and h_0 is an idealized means to represent that elliptical shape. If h_0 is small, pore is like a crack and it can grow faster under normal, mode-I, loading. The influence of these parameters on the traction-separation response can be seen in Figs. 4 and 5.

At this stage, it is convenient to recapitalize important characteristics of the proposed TSLs as follows:

- Eqs. (15) and (18) reveal that normal and tangential components of the traction depend on micromechanical variables in different ways. To be more precise, mode-I traction separation law has a logarithmic dependency on the inverse of initial pore fraction f_0 which results in very high strength values as f_0 diminishes. On the other hand, tangential traction has a power type dependency which typically yields much smaller initial tangential strength as compared to normal one, see Figs. 4 and 5. This has important implications on the initiation and evolution of cohesive cracks along the grain boundaries.
- It is clearly seen that tangential traction is insensitive to initial pore height h_0. On the contrary, due to logarithmic nature of the dependency of T_n on h_0, post-peak response of T_n is highly sensitive to h_0 as can be seen in Fig. 4. As h_0 increases (for constant h_0), the drop of T_n becomes smoother which in turn influences the evolution of the normal opening.
- As far as the influence of pore spacing l is concerned, a power type dependency of T_t on l is apparent. For constant initial pore volume f_0, reducing the pore spacing leads to lower fracture energies, see Fig. 5. In other words, larger number of smaller pores require lower energy than a smaller number of larger pores.

It has to be re-emphasized that the cohesive strength, energy and the dependency of normal and tangential tractions on the associated separations are the outcomes of the void growth based micromechanical model.

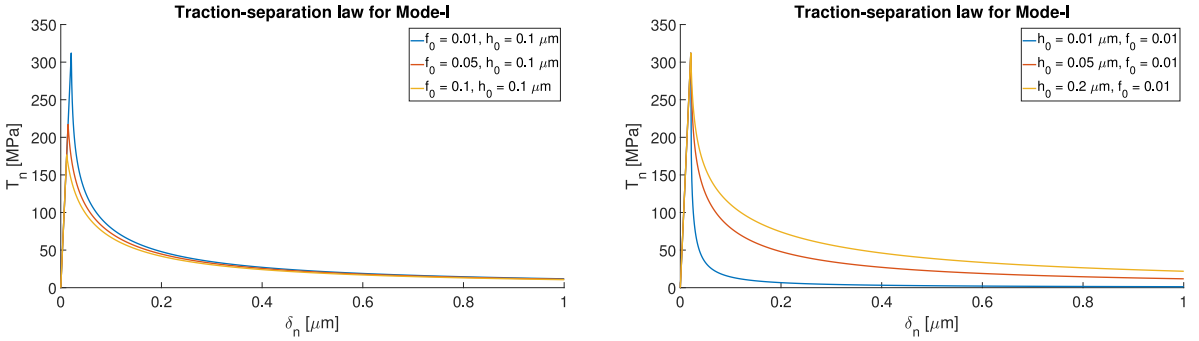

Fig. 4. Mode-I traction-separation behavior of MBCZM for $\sigma_y = 110$ MPa and different values of f_0, h_0.

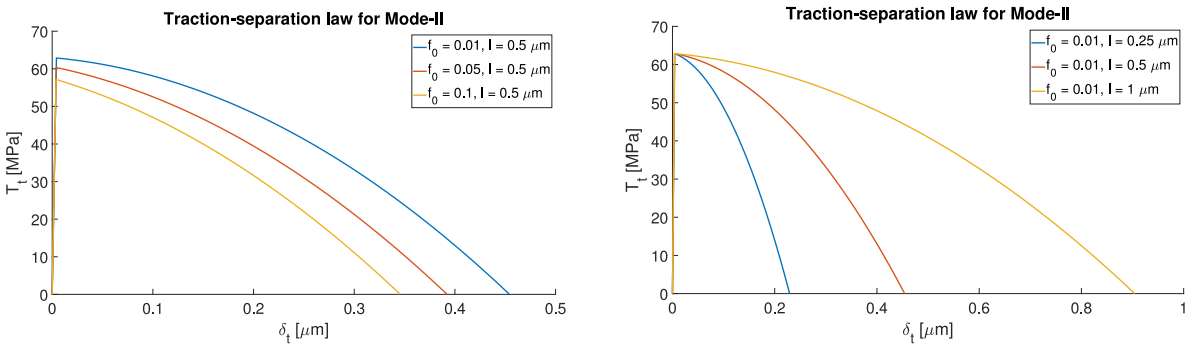

Fig. 5. Mode-II traction-separation behavior of MBCZM for $\sigma_y = 110$ MPa and different values of f_0, l.

Table 1
PPR model parameters corresponding to the traction-separation behavior presented in Figs. 4 and 5.

f_0 for a constant $h_0 = 0.1$ μm	Φ_n [N/m]	Φ_t [N/m]	σ_{max} [MPa]	τ_{max} [MPa]	α	β	λ_t	λ_n
$f_0 = 0.01$	53.2	18.3	312.1	62.9	19.1	1.8	0.005	0.111
$f_0 = 0.05$	46.1	14.6	217.1	60.3	15.1	1.8	0.005	0.081
$f_0 = 0.1$	42.9	11.9	176.6	57.2	13.1	1.8	0.005	0.081
h_0 for a constant $f_0 = 0.01$	Φ_n [N/m]	Φ_t [N/m]	σ_{max} [MPa]	τ_{max} [MPa]	α	β	λ_t	λ_n
$h_0 = 0.01$ μm	14.5	18.3	312.1	62.9	109.1	1.8	0.005	0.111
$h_0 = 0.05$ μm	34.7	18.3	312.1	62.9	31.1	1.8	0.005	0.111
$h_0 = 0.2$ μm	96.7	18.3	312.1	62.9	21.1	1.8	0.005	0.111

2.2.5. *Fitting of TSL for mixed-mode loading*

In order to reduce the implementation and computational cost, for the mixed-mode simulations, the TSL of previously developed Micromechanics Based Cohesive Zone Model (MBCZM) is fitted to Park–Paulino–Rosler (PPR) cohesive zone model (Park et al., 2009) separately for mode-I and mode-II. In PPR traction separation relations are characterized by the following variables: ϕ_n, ϕ_t, normal and tangential fracture energies, σ_{max}, τ_{max} normal and tangential cohesive strengths, α, β, shape parameters, λ_n, λ_t normal and tangential initial slope indicators. Corresponding parameters in PPR are obtained for given f_0, h_0, and l parameters in MBCZM. In the fits, it is made sure that the two important parameters of a TSL are as close as possible. Namely, maximum traction and fracture energy, i.e. the area under the curves. The obtained parameters are given in Table 1. In this way, the effect of microstructural parameters such as h_0 and f_0 can be investigated in the inter-granular fracture of polycrystalline specimens.

2.2.6. *Finite element models*

A ten-noded tetrahedra element with quadratic displacement and linear slip interpolation is implemented in Abaqus through user element (UEL) subroutine and used for the discretization of the grains. For the cohesive fracture of grain boundaries, three dimensional twelve noded (six on each side of the potential discontinuity) zero thickness interface element of Cerrone et al. (2014) is used which is compatible with the displacement interpolation used in the bulk elements. As presented in the next section, models with different number of grains are considered resulting in different number of elements. In order to assess the convergence of the model predictions upon mesh refinement, a model with ten grains are analyzed with three different mesh density. The details of the model in terms of material parameters and boundary conditions are presented in Section 3. The resulting stress–strain graphs

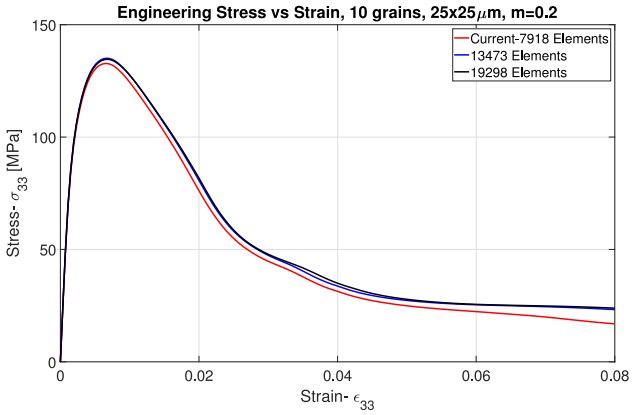

Fig. 6. Engineering stress vs. strain response of a polycrystalline cylindrical specimen with 25 μm diameter and 25 μm length including 10 grains deformed under tensile loading for changing mesh density.

Table 2
Material properties of the strain gradient crystal plasticity model.

Young modulus E [MPa]	Poisson ratio ν [-]	Reference slip rate $\dot{\gamma}_0$ [s^{-1}]	Slip resistance s [MPa]	Orientations [°]	Material length scale R[μm]	m [-]
70000.0	0.33	0.001	25.0	Random	0.4	0.2

shown in Fig. 6 supports that the predictions of the material models and the elements employed converge upon mesh refinement. However, the computational cost increases enormously as the number of grains increases which has inhibited the use of very fine meshes for models with large number of grains (> 50).

3. Numerical results

In this section the numerical performance of the physics based inter-granular ductile fracture framework is illustrated through different microstructural parameters on micron size specimens generated using Voronoi tesselation. The simulations are conducted for a cylindrical specimen deformed under uniaxial tensile and shear loading. The back surface of the specimen is fixed, i.e. displacements $u_{1,2,3}$ and rotations $u_{R1,2,3}$ are set to zero. The front face is free to move, where the displacement boundary conditions are specified (see Fig. 7). The plastic slips are set to zero at both free and fixed surfaces. For bulk plasticity response of grains strain gradient crystal plasticity model is used through an Abaqus user element subroutine while PPR cohesive zone elements are inserted at intergranular faces, which work through another Abaqus UEL (see Cerrone et al., 2014). Material parameters for SGCP are given in Table 2 and cohesive zone parameters for PPR-CZM are given in Table 1. The slip resistance is taken as constant without hardening in order not to overcomplicate the interaction of several complex mechanisms. Suppressing bulk hardening allows us to better interpret the effects of micromechanical parameters from cohesive zone model on results. The hardening observed in the material arises completely due to non-local effect and in this way the formulation is consistent with the cohesive zone framework which considers rigid perfect plastic matrix material. Note that the analysis is purely qualitative and does not have the purpose of conducting any comparison with experimental data. However, it presents crucial conclusions on the micromechanisms of ductile intergranular cracking.

Orientation difference among the grains and the induced deformation incompatibility at the grain boundaries results in traction increase at the grain boundaries, which in turn affects the evolution of existing porosity through the presented formalism in the previous section. The potential based cohesive zone elements take into account the influence of cavity evolution under the mixed mode loading conditions. The framework considers solely the weakening of the grain boundaries where the precipitate free zones (PFZ) nearby the grain boundary is soft compared to grain interior and deforms first plastically under large triaxiality constrained by the harder grains. This physical mechanism leading to large void growth rate is included in the model through the micromechanics based cohesive zone relations. The other scenario when the grains yield before the onset of coalescence in the PFZ that would eventually lead the damage inside grains before the GBs, resulting in transgranular cracking is not taken into account in the current study. However, the micromechanical analysis of both non-local plasticity in the grains as well as the damage between the grains through physics based relations and the analysis of the influence of the microstructural parameters on the ductile fracture response of such materials have not been done in the open literature yet. The current examples present crucial conclusion on the toughness of the micron sized specimens that suffer grain boundary weakening. All the computations are conducted in Abaqus software, where Neper (Quey et al., 2011) is employed for the generation of grain microstructure in the pre-processing step. The insertion of the cohesive zone elements and the illustration of the results in Abaqus are conducted through the developed scripts.

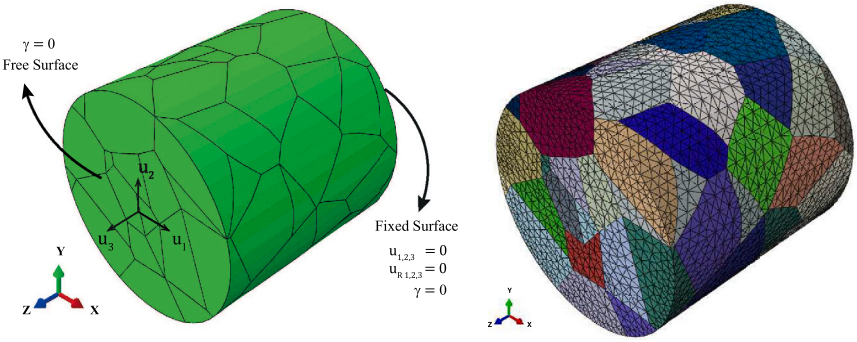

Fig. 7. The representation of the boundary value problem with 100 grains and finite element mesh.

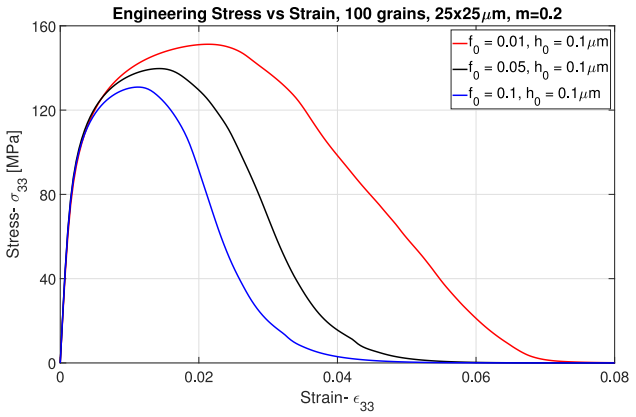

Fig. 8. Engineering stress vs. strain response of a polycrystalline cylindrical specimen with 25 μm diameter and 25 μm length including 100 grains deformed under tensile loading for variable initial pore fraction, f_0 and constant initial pore height, h_0.

3.1. The effect of initial porosity f_0 at the grain boundaries

The initial example addresses the influence of porosity at the grain boundaries on both macroscopic constitutive response and spatial stress and strain evolution in a specimen with 25 μm diameter and 25 μm length including 100 grains. In order to illustrate this phenomenon three different initial porosity ratios are considered, i.e. $f_0 = 0.01$, $f_0 = 0.05$, $f_0 = 0.1$ for a constant pore height $h_0 = 0.1$ μm. The stress–strain response of the specimen deformed under uniaxial tension is presented in Fig. 8. At the hardening stage three specimens show identical behavior, however, as expected, the ones with higher porosity start softening earlier due to their lower cohesive strengths as depicted in Figs. 4 and 5. There is considerable reduction in the toughness of the material with increasing grain boundary cavity ratio. Then contour plots of stress and strain are illustrated at peak engineering stress and at 8% global strain state in Figs. 9 and 10, respectively. Fig. 9 shows that at peak stress state, the case with the lowest porosity reaches to highest stress at the grain boundaries and highest strain in the grains. When the cracked specimens are analyzed in Fig. 10, the crack initiation locations for high porosity grain boundary microstructure ($f_0 = 0.05$ and $f_0 = 0.1$) are identical. However, it is different for the lowest porosity case, which means even though the initial cavity is distributed homogeneously at all grain boundaries the crack initiation location might depend on the level of the porosity. Therefore the interaction between the orientation mismatch and the cavity ratio influence both toughness and the crack path in the specimen. Referring back to the main characteristics of TSLs of MBCZM, particularly at low f_0 levels, the initiation of mode-II type opening would be easier. Therefore, the deviation observed locally in crack path for $f_0 = 0.01$ seems to be consistent with this characteristic. For relatively larger f_0 values, the crack 'prefers' the neighboring path which is almost pure mode-I opening whereas for $f_0 = 0.01$, mode-II dominated inclined crack path emerges.

3.2. The effect of cavity height h_0 (pore shape) at the grain boundaries

The next example addresses the influence of cavity height parameter at the grain boundaries on the macroscopic constitutive response and the spatial stress and strain evolution in the same specimen. The effect is studied at constant porosity levels. When $f_0 = 0.01$ and $h_0 = 0.2$ μm, the pore radius is $a = 0.1$ μm which corresponds to a spherical pore. However, if the pore height is reduced, it takes an ellipsoid shape and the pore geometry looks more like a crack and it would be easier to initiate and to propagate the cracks with that cavity geometry under mode I loading. This parameter does not have any effect on mode II fracture characteristics

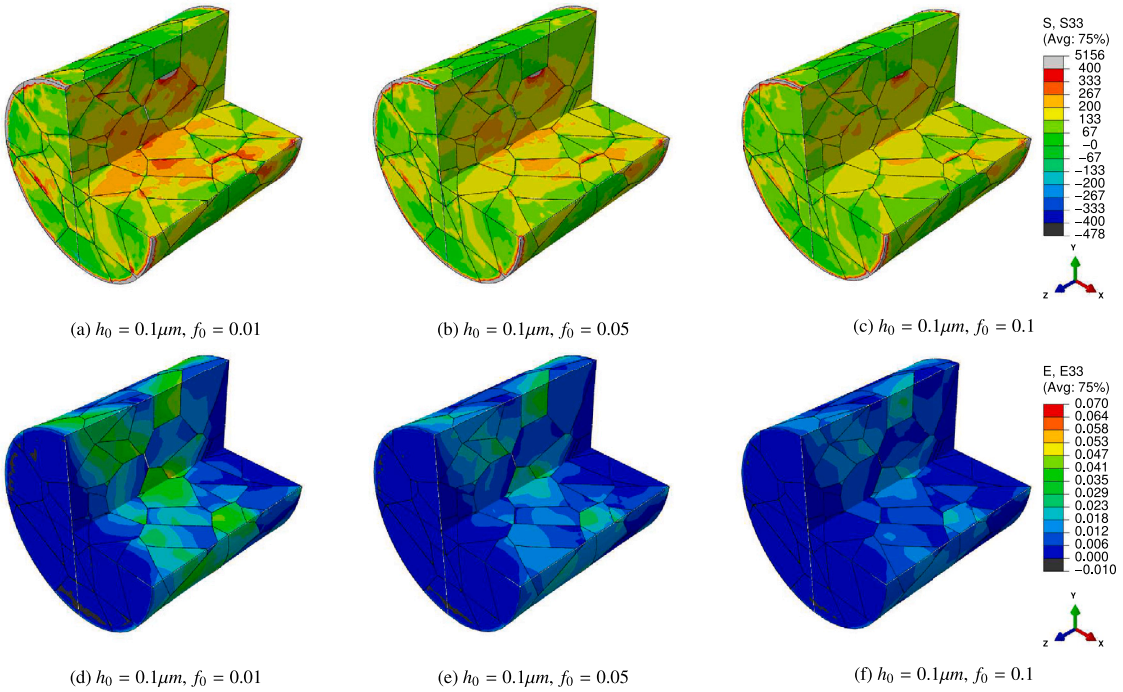

(a) $h_0 = 0.1\mu m$, $f_0 = 0.01$ (b) $h_0 = 0.1\mu m$, $f_0 = 0.05$ (c) $h_0 = 0.1\mu m$, $f_0 = 0.1$

(d) $h_0 = 0.1\mu m$, $f_0 = 0.01$ (e) $h_0 = 0.1\mu m$, $f_0 = 0.05$ (f) $h_0 = 0.1\mu m$, $f_0 = 0.1$

Fig. 9. Contour plots for the stress (σ_{33}) (a, b, c) and strain (ϵ_{33}) (d, e, f) at the peak engineering stress increment for different initial pore fractions, $f_0 = 0.01$ (a, d), $f_0 = 0.05$ (b, e), $f_0 = 0.1$ (c, f).

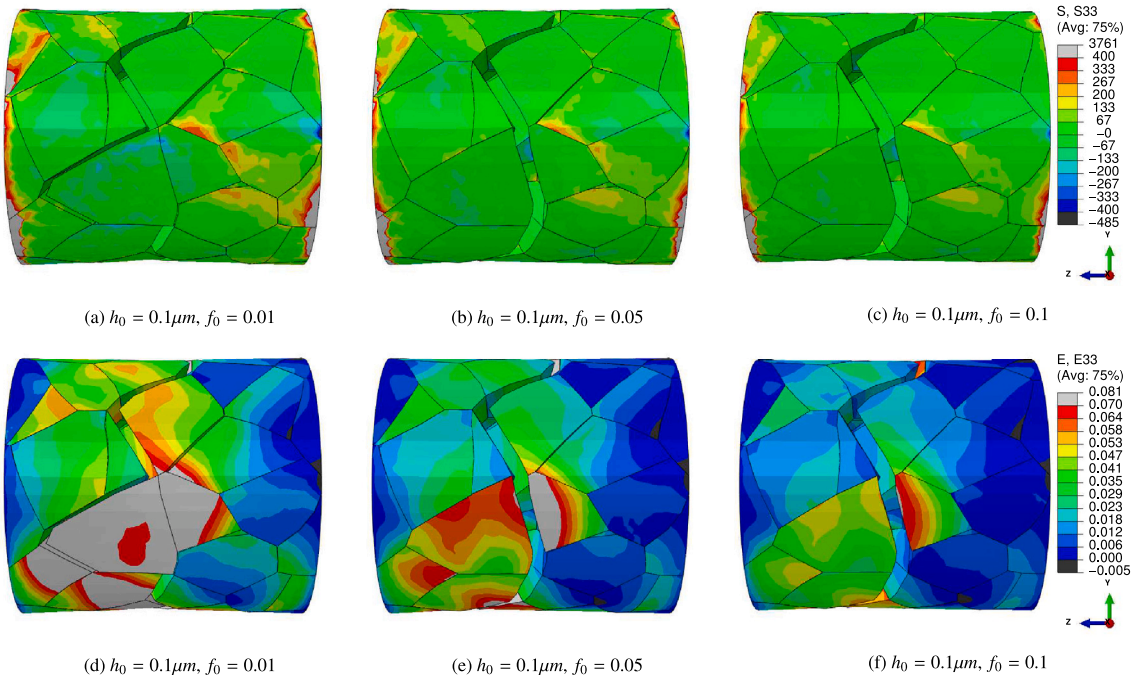

(a) $h_0 = 0.1\mu m$, $f_0 = 0.01$ (b) $h_0 = 0.1\mu m$, $f_0 = 0.05$ (c) $h_0 = 0.1\mu m$, $f_0 = 0.1$

(d) $h_0 = 0.1\mu m$, $f_0 = 0.01$ (e) $h_0 = 0.1\mu m$, $f_0 = 0.05$ (f) $h_0 = 0.1\mu m$, $f_0 = 0.1$

Fig. 10. Contour plots for the stress (σ_{33}) (a, b, c) and strain (ϵ_{33}) (d, e, f) at 8% global strain for different initial pore fractions, $f_0 = 0.01$ (a, d), $f_0 = 0.05$ (b, e), $f_0 = 0.1$ (c, f).

within the current formulation. Higher cavity height hinders the crack propagation giving higher toughness. The effect is clearly illustrated in Fig. 11 on macroscopic stress–strain curves, where smaller cavity height results in early softening and cracking. The

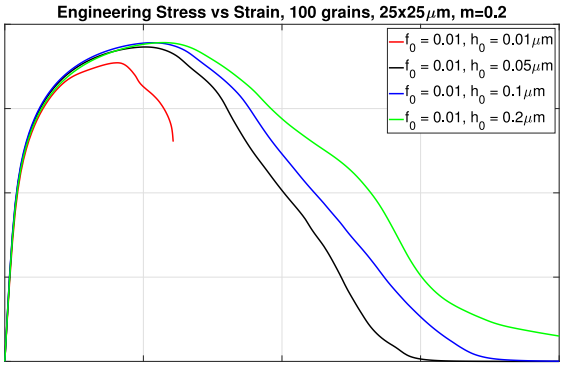

Fig. 11. Engineering stress vs. strain response of a polycrystalline cylindrical specimen with 25 μm diameter and 25 μm length including 100 grains, deformed under tensile loading for variable initial pore height, h_0, and constant initial pore fraction, f_0.

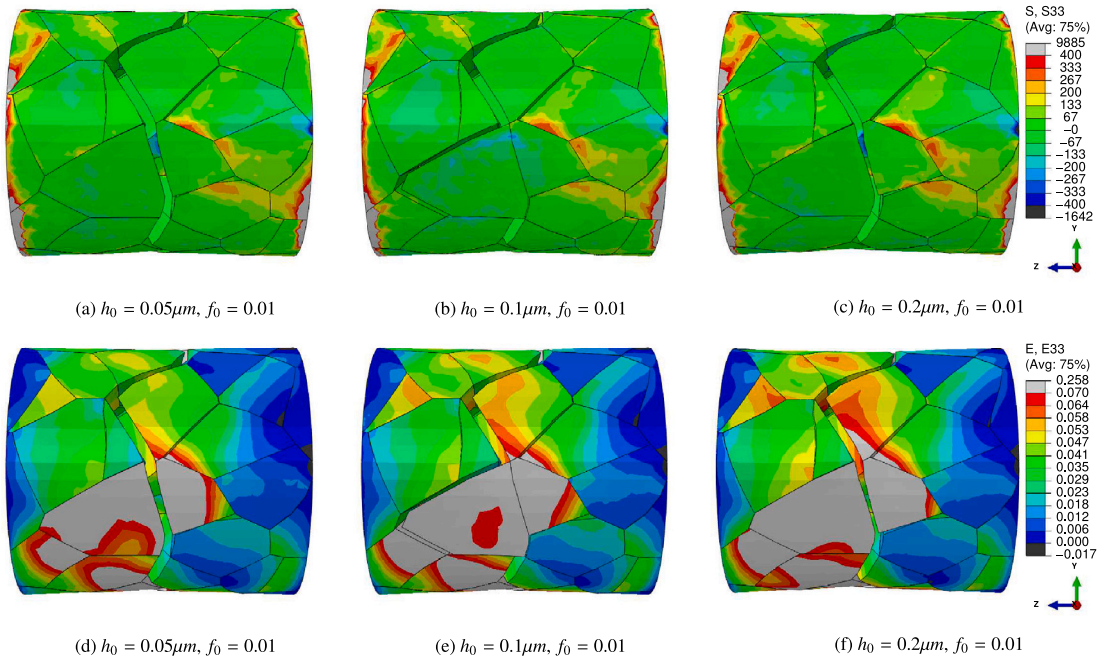

(a) $h_0 = 0.05\mu m$, $f_0 = 0.01$ (b) $h_0 = 0.1\mu m$, $f_0 = 0.01$ (c) $h_0 = 0.2\mu m$, $f_0 = 0.01$

(d) $h_0 = 0.05\mu m$, $f_0 = 0.01$ (e) $h_0 = 0.1\mu m$, $f_0 = 0.01$ (f) $h_0 = 0.2\mu m$, $f_0 = 0.01$

Fig. 12. Contour plots for the stress (σ_{33}) (a, b, c) and strain (ε_{33}) (d, e, f) at peak engineering stress increment for different initial pore height, $h_0 = 0.05$ (a, d), $h_0 = 0.1$ (b, e), $h_0 = 0.2$ (c, f).

contour plots of stress and strain distribution corresponding to 8% global strain are given in Fig. 12. It is interesting to note that similar to f_0, h_0 has an effect on the crack path as can be seen in Fig. 12. Since smaller h_0 values make the interface more mode-I fracture prone, a mode-I type crack profile is visible at exactly the same grain boundary shown in Fig. 10. However when h_0 is raised to 0.2 μm, the local fracture at the same spot regains a mode-I character. Although it is difficult to explain this behavior with the main characteristics of MBCZM, this is probably related with the modified opening profiles in the neighborhood of this spot (see Fig. 12(c)). Larger h_0 prevents abrupt drop in normal traction and therefore open up more room for normal and tangential sliding before local failure of the interface. Such local crack opening differences lead to the wavy profile observed in post-peak region of stress–strain graph given in Fig. 11, particularly for $h_0 = 0.2$ μm.

3.3. The effect of porosity f_0 and pore height h_0 under shear loading

In this example the effect of both pore fraction and the pore height on inter-granular ductile fracture is studied under shear loading in the specimen of previous examples. The stress–strain response curves are presented in Fig. 13 for both variable porosity

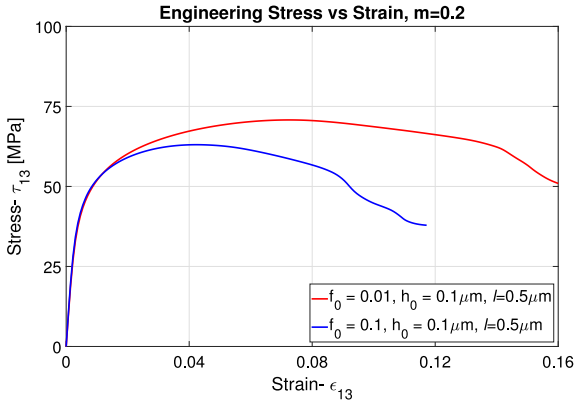

(a) Variable initial pore fraction f_0.

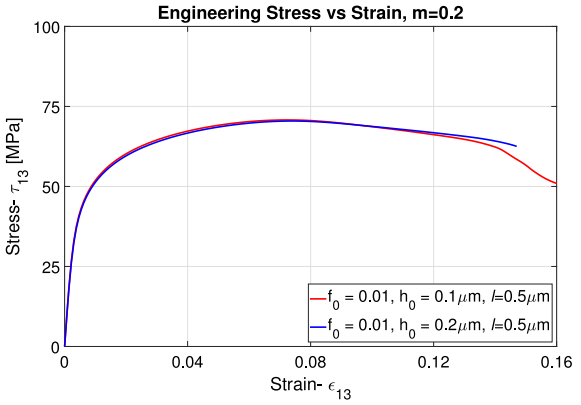

(b) Variable initial pore height h_0.

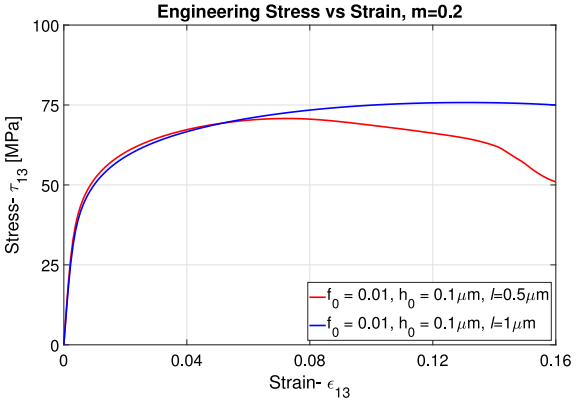

(c) Variable initial pore spacing l.

Fig. 13. Engineering stress vs. strain response of a polycrystalline cylindrical specimen with 25 μm diameter and 25 μm length including 100 grains, deformed under shear loading for variable initial pore fraction f_0 (a), variable initial pore height h_0 (b) and variable initial pore spacing l (c).

with constant pore height and for variable pore height with constant porosity. In these examples, it is not possible to conduct simulations till complete fracture with full softening due to convergence issues coming from the complications of grain interactions, e.g. closure of interface elements and large penetrations. The graphs are plotted until the last converged increment. Moreover, in this mode of loading more deformation is required compared to tensile case to cause full failure, since there is more resistance by the body of grains in shear direction, i.e., the grains are pushing each other. The adverse effect of porosity on fracture behavior under shear loading is clearly visible in Fig. 13(a). Since mode-II failure is insensitive to pore height, almost coincident stress–strain graphs are obtained for two different h_0 values as shown in Fig. 13(b). At the final stages of loading (e.g. $\epsilon_{13} > 0.12$) mixed-mode failure of certain grain boundaries dominate and the two curves start to divert. Probably a more interesting result is obtained when the pore spacing is halved while initial pore fraction is kept constant. The resulting stress–strain graphs presented in Fig. 13(c) clearly show that smaller pore spacing leads to much earlier onset of softening. In other words, larger number of smaller voids within a representative volume is more detrimental than larger but fewer voids. In Fig. 14, the resulting stress distribution corresponding to the last stage of loading are shown for two different pore spacing cases. The openings and sliding of the grain boundaries are much more severe for $l = 0.5$ μm which is totally consistent with the softening observed.

3.4. Grain orientation distribution

The next example investigates the influence of grain orientations on both the macroscopic and microscopic behavior of micron sized samples under uniaxial loading. Five different random orientation sets are assigned to the grains of the sample with 100 grains, and the engineering stress–strain responses are plotted in Fig. 15(a). There is no substantial difference in the hardening region due to the high number of grains in the specimen, which means the orientation influence of individual grains is almost negligible and the extrinsic size effect does not exist. However the influence of different orientation sets is more visible at the peak stress and in the softening region. The reason behind this difference can well be explained by stress and strain contour plots presented in Fig. 16 at 8% global strain level where a complete failure is obtained in each case. The figures show that the crack path is different for different orientation sets which is illustrated for sets 1, 4 and 5. This is an expected result since the stress concentrations at

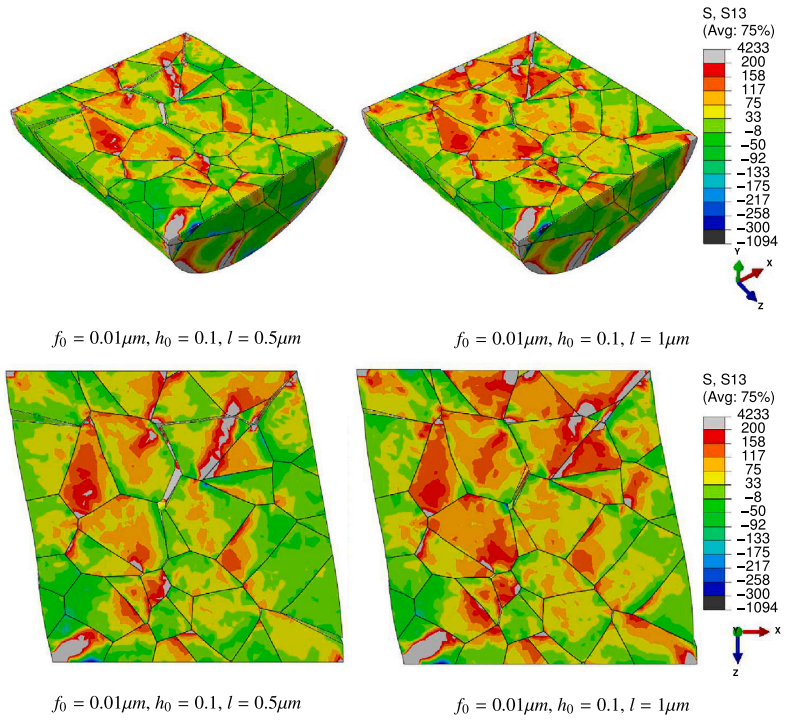

Fig. 14. Contour plots of σ_{13} under shear loading for different l conditions at the last converged strain.

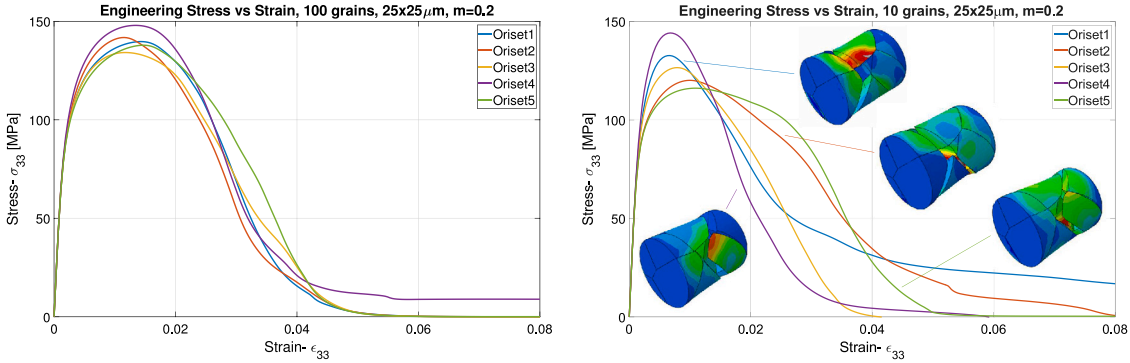

(a) Sample with 100 grains.

(b) Sample with 10 grains.

Fig. 15. Engineering stress vs. strain response of a polycrystalline cylindrical specimen with 25 μm diameter and 25 μm length including 100 grains (a) and 10 grains (b), deformed under tensile loading for different sets of randomly generated grain orientations.

the grain boundaries are purely orientation mismatch dependent, which is distinct for different orientation distribution, inducing different traction levels at the same locations for the same specimen. The influence of the grain orientation on the micro crack formation and propagation has recently been discussed by the authors through phenomenological traction separation relations as well (see Yalcinkaya et al., 2019). It has been shown that even if the orientation set is identical, different random distribution in specimen results in similar observation where the micro specimen with the same pole figure shows different fracture characteristics. For comparison reason, another case with 10 grains is analyzed again under same loading conditions for 5 different orientation sets and the results are presented in Fig. 15(b). The macroscopic response shows a strong extrinsic size effect where the orientation of individual grains dominate both hardening and softening regimes in the constitutive response. Moreover the crack paths of the specimens with 10 grains are also presented in the same figure which shows a strong orientation dependence as well, which is also a valid observation for the material toughness.

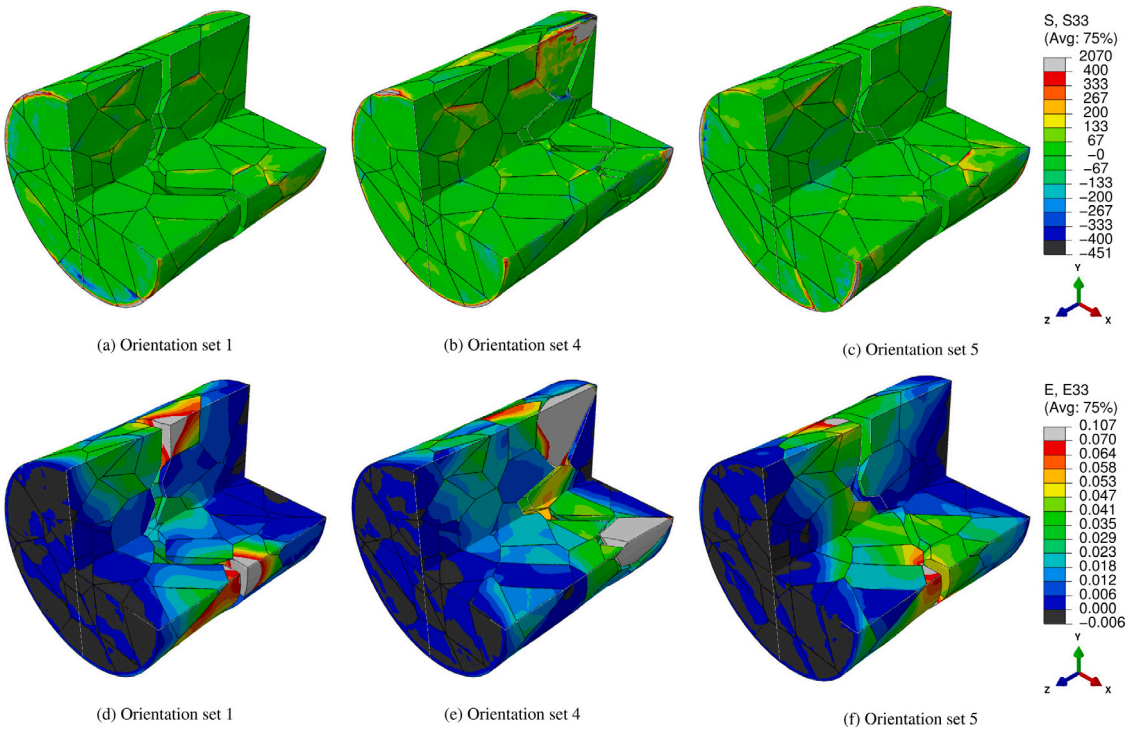

Fig. 16. Contour plots for the stress (σ_{33}) (a, b, c) and strain (ϵ_{33}) (d, e, f) at 8% global strain level for different orientation sets: set 1 (a, d), set 4 (b, e), and set 5 (c, f).

3.5. Grain boundary conditions

The coupled finite element solution framework implemented here for the nonlocal higher order plasticity model allows the description of boundary conditions at the grain boundaries in terms of plastic slip. The classical local theories of crystal plasticity do not impose any condition of plasticity at the boundaries. However, the grain boundary dislocation interactions are quite complicated and should be taken into account in a coarse grained manner at this length scale. There has been a number of models considering this phenomenon, which do not consider only the conventional boundary conditions such as hard boundaries, with $\gamma = 0$ or soft (micro-free or traction-free) boundaries, but also take into account the flexible conditions where the cases in between these two limiting situations are considered (see e.g. Özdemir and Yalcinkaya, 2019) through a grain boundary model based on micromechanics of grain boundary dislocation interactions (see e.g. Gurtin, 2008; van Beers et al., 2013; Özdemir and Yalçinkaya, 2014; Benedetti et al., 2016; Alipour et al., 2019; Voyiadjis and Song, 2019; Yalçinkaya et al., 2021). In the current study, dislocation slip–grain boundary interaction is handled through continuous slip and limiting cases such as free slip (micro-free) and hard boundary (zero slip) conditions. In case of continuous slip, the slip fields are forced to be continuous across the grain boundaries regardless of the fact that neighboring grain orientations are different. Hard boundary condition corresponds to complete blockage of dislocations at the grain boundaries whereas micro-free grain boundaries are the ones where the associated interfacial tractions (λ_A^α and λ_B^α) are zero. In other words, in case of micro-free boundary condition, dislocation slip reaches to a traction free internal surface and does not 'feel' the existence of the neighboring grain. In Fig. 17 the engineering stress–strain curves for a polycrystalline specimen with 100 randomly oriented grains are presented for different boundary conditions with $h_0 = 0.1 - 0.2$ μm and $f_0 = 0.01$. The results show a strong boundary condition dependence of both plasticity and fracture behavior in the specimen.

In Fig. 18 the contours of stress (σ_{33}) and strain (ϵ_{33}) are presented for soft, continuous and hard grain boundary conditions at the peak engineering stress increment. Till the point softening starts, the stress concentrations at the grain boundaries are highest for the hard boundary condition case, followed by the continuous and soft cases, which is obvious in the macroscopic response shown in Fig. 17 as well. Therefore the cracks are initiated first in the hard boundary case and the material starts to soften while the other two cases are still hardening. In a short while the softening starts in the continuous and soft boundary cases as well, and the cracks are initiated at the same locations in all conditions, which basically depends on the orientation mismatch. Hard boundary conditions make the specimen more prone to failure and lead to minimum toughness. The complete fracture occurs at substantially low plastic strain for hard grain boundary condition case followed by the continuous and soft grain boundary conditions. For the soft boundary condition case, much higher plastic strain levels are required before the failure. The contour plots reveal that the hard boundary condition is a strong one enforcing the slip values to be zero at the grain boundaries leading to low plastic strain values all over the specimen which in turn increases the stress levels substantially. In the continuous case the continuity of plastic slip is

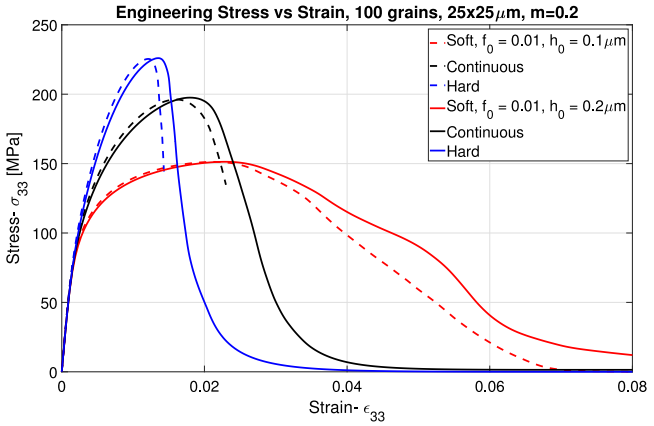

Fig. 17. Engineering stress vs. strain response of a polycrystalline cylindrical specimen with 25 μm diameter and 25 μm length including 100 grains, deformed under different boundary conditions and for $h_0 = 0.1 - 0.2\mu m$ and $f_0 = 0.01$.

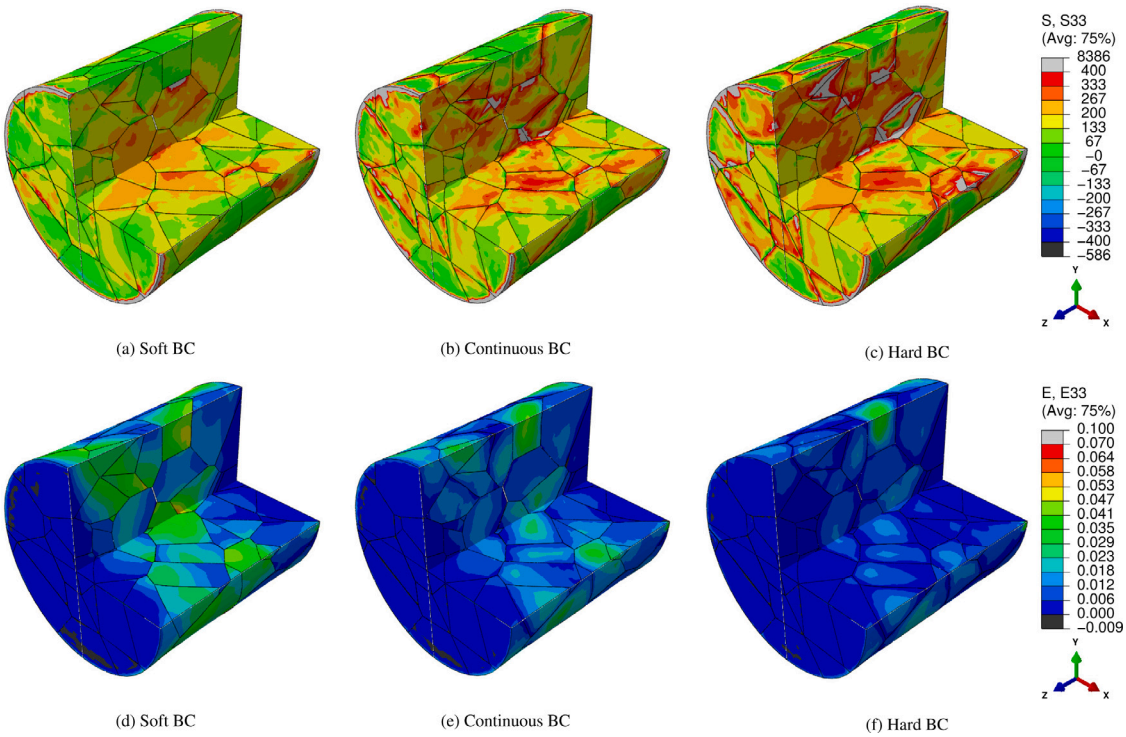

Fig. 18. Contour plots for the stress (σ_{33}) (a, b, c) and strain (ϵ_{33}) (d, e, f) at the peak engineering stress increment for different boundary conditions Soft BC (a, d), continuous BC (b, e) and hard BC (c, f).

implemented at the GBs relaxing the evolution of the plastic strain. For soft boundary conditions the jumps in the plastic slip values are induced as observed in the local crystal plasticity models. The plasticity evolves rather easily and the stress concentrations are considerably less than the other cases. The toughness of the material is maximum for the case with soft grain boundary conditions.

3.6. The effect of non-random orientation distribution

In the previous examples the orientation distributions of the grains are taken to be random, and the effects of various microstructural parameters are analyzed in detail. In this example, the randomness of the orientations is restricted and a kind of texture is given to the model by restricting the orientation distribution. In this context, in addition to the random case, the situations where the orientations are confined to 30–35°, 40–45° and 70–75° are addressed in a longer specimen with 25 μm diameter and 50 μm length including 100 grains. The engineering stress versus strain response of the specimen for two different m values are

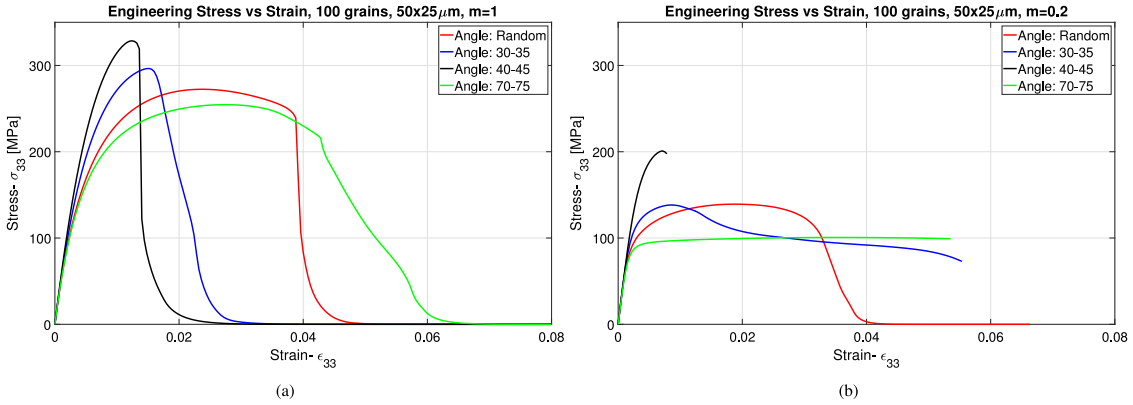

Fig. 19. Engineering stress vs. strain response of a polycrystalline cylindrical specimen with 25 μm diameter and 50 μm length including 100 grains, deformed under tensile loading for random and non-random orientation distribution cases for $m = 1$ (a) and $m = 0.2$ (b).

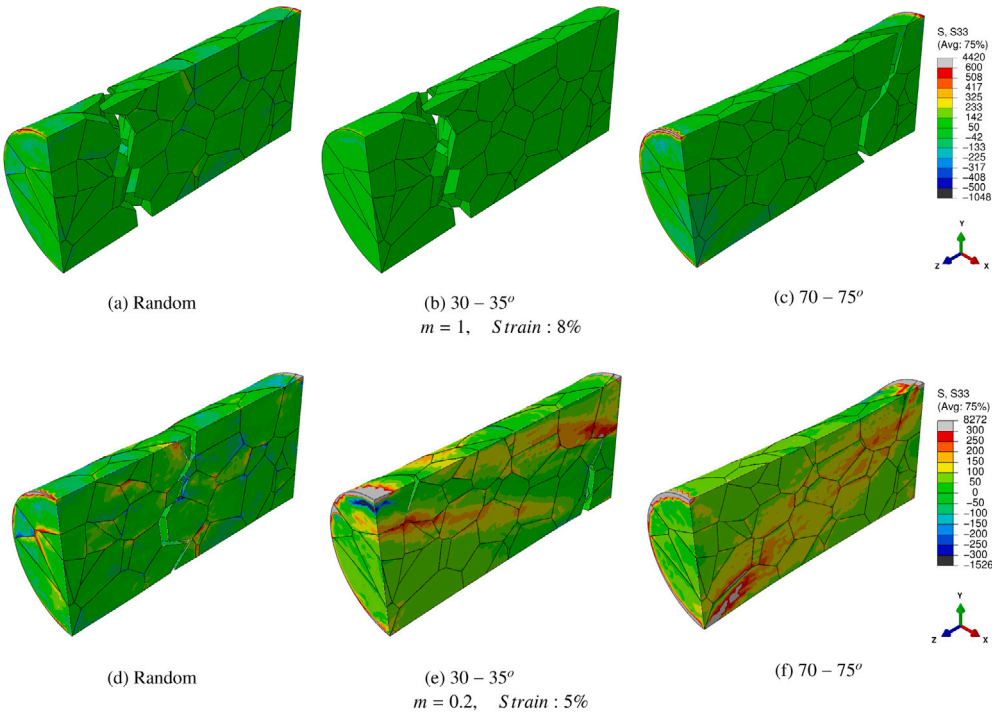

Fig. 20. Contour plots for the stress (σ_{33}) at 8% global strain level and $m = 1$ (a, b, c) and at 5% global strain level and $m = 0.2$ (d, e, f) for random and restricted orientation distributions.

presented in Fig. 19. In case of $m = 1$, the evolution of the plastic strains are rather slow as compared to $m = 0.2$ and because of that the resulting stress values are higher. Higher stresses in turn induce sufficiently large tractions at the grain boundaries and even in case of low orientation variations, the failure within the span is feasible, as exemplified in Fig. 20(b). However, for $m = 0.2$, the stresses are rather low within the span. In this case, the heterogeneity induced by the mechanical boundary conditions make the regions closer to the boundaries more prone to fracture. In fact, for $m = 0.2$, fracture initiates at grain boundaries which are close to the fixed end and at some stage of loading the evolving crack tends to intersect with the surface which is totally fixed. This results in sustained stress levels and sometimes very slow stress decay as can be seen in Fig. 19(b). This observation calls for alternative boundary conditions or specimen shapes/sizes by which non-randomness of grain orientations can be investigated. The tendency of failure in the end regions is also observed for $m = 1$ and when the orientations are confined to 70–75°. Since the orientation of the grains are approaching to the loading axis, the stress levels are getting smaller as compared to other confined orientation ranges and a similar situation to $m = 0.2$ arises.

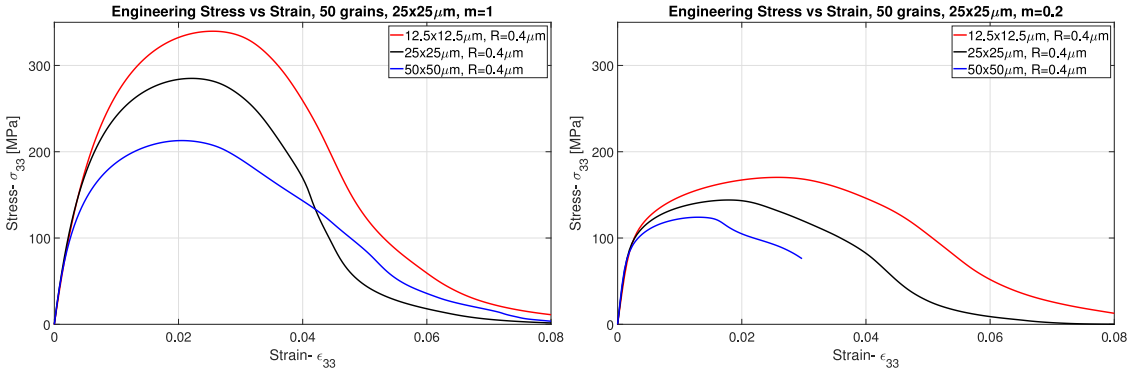

Fig. 21. Engineering stress vs. strain response of a polycrystalline cylindrical specimen with different dimensions: 12.5 μm × 12.5 μm, 25 μm × 25μm and 50 μm × 50 μm, including 50 grains deformed under tensile loading where $m = 1$ (left) and $m = 0.2$ (right).

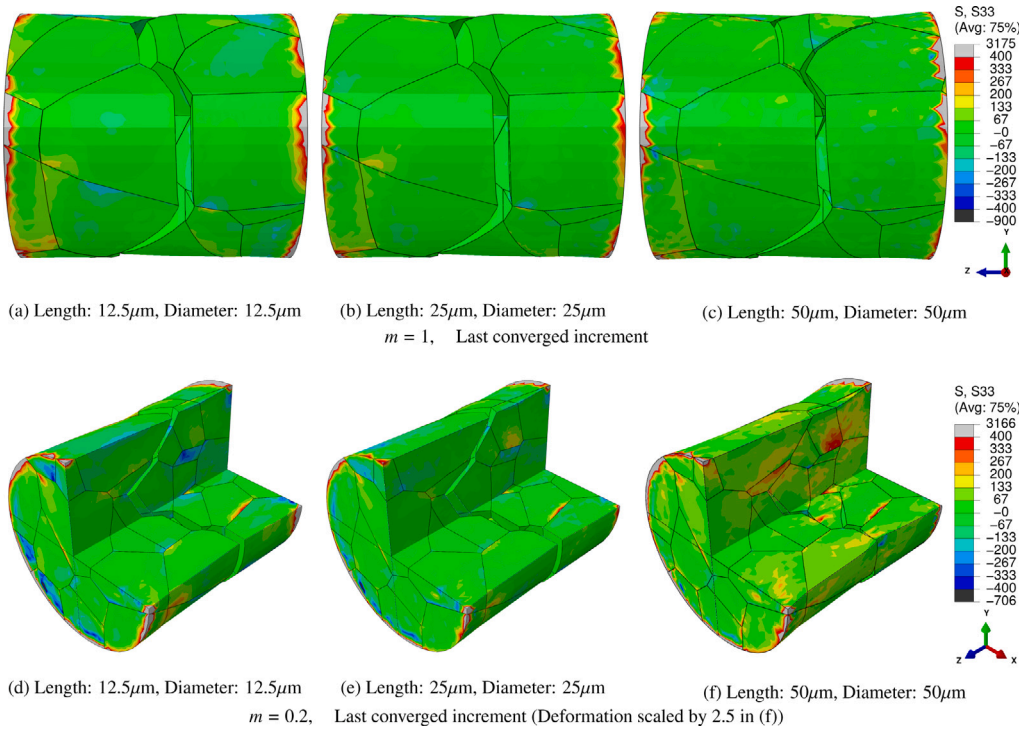

(a) Length: 12.5μm, Diameter: 12.5μm (b) Length: 25μm, Diameter: 25μm (c) Length: 50μm, Diameter: 50μm

$m = 1$, Last converged increment

(d) Length: 12.5μm, Diameter: 12.5μm (e) Length: 25μm, Diameter: 25μm (f) Length: 50μm, Diameter: 50μm

$m = 0.2$, Last converged increment (Deformation scaled by 2.5 in (f))

Fig. 22. Contour plots of the stress (σ_{33}) at last converged global strain increment in cylindrical specimens including 50 grains with different dimensions: 12.5 μm × 12.5 μm, 25 μm × 25 μm and 50 μm × 50 μm, and for $h_0 = 0.2$ μm and $f_0 = 0.01$.

3.7. Size effect

The last example is concerned with the size effect response of the micron sized specimens. It is expected that smaller specimens should show a stronger response because of the Hall–Petch effect. Due to the nature of the non-local strain gradient crystal plasticity model this effect can be simulated simply by changing the geometrical size of the specimen, or by changing the length scale parameter, R. The influence of specimen size is presented in Fig. 21 for two different m values. Three different specimen sizes of 25 μm by 25 μm, 12.5 μm by 12.5 μm and 50 μm by 50 μm are considered. For both m values, the classical strain gradient effect is clearly observable. Both the peak stress and the hardening slope are larger for smaller specimen. Significantly different normal stresses for different m values are essentially due to smaller plastic strain levels reached for $m = 1$. Apart from that, the differences in peak stresses for different specimen sizes are also notable. This is probably the reason to get different crack paths for different specimen sizes as shown in Fig. 22. As the stress level varies, the normal and tangential tractions driving the openings of grain boundaries differ and this in turn leads to local crack path changes as shown in Figs. 22(c) and 22(f).

4. Conclusions and outlook

In this paper, a micromechanics based traction-separation model is derived, and its performance is investigated numerically through cohesive zone elements together with a strain gradient crystal plasticity model in the context of intergranular ductile fracture observed in various high strength aerospace alloys. The effects of various microstructural parameters are analyzed in detail and the key findings of the study are listed below.

- There is a substantial effect of the initial pore fraction at the grain boundaries in the failure behavior of the material, while there is no influence at the early hardening phase. The case with higher porosity starts softening earlier and results in lower toughness. The case with lowest porosity reaches the highest stresses at the grain boundaries and the highest strain in the grains. Porosity affects the crack path as well, due to the complicated interaction between orientation mismatch induced local stress concentrations and pore fraction dependent cohesive response.
- The analysis of the pore shape reveals that higher cavity height results in higher toughness hindering the crack propagation under tensile loading. When the pore height is reduced, the shape of the pores resembles an ellipsoid (i.e. scaling a sphere in pore height direction) which in turn leads to early softening and cracking. Similar to f_0, initial pore height h_0 affects the crack path as well. Inclined grain boundary surfaces with respect to loading direction inevitably induces mixed-mode openings in many grain boundaries and any change in normal and/or tangential traction response might lead to crack path changes. In this particular case, initial pore height influences the normal traction response and triggers crack path changes. Pore shape does not have any practical influence for mode II fracture.
- It is interesting to note that, under shear loading, pore spacing l changes the response significantly although the initial pore fraction is the same. Higher number of smaller pores initiates softening much earlier.
- For the case with relatively high number of grains, e.g. 100, the change in the random orientations does not lead to a considerable influence in the plasticity and fracture behavior. The larger differences in the softening part compared to the hardening one is due to the change in the crack path. Both macroscopic and microscopic responses are highly orientation dependent in the samples with less number of grains, where the extrinsic size effect plays an important role in both plasticity and fracture behavior.
- The hard boundary conditions for plasticity at the grain boundaries ($\gamma = 0$) results in higher hardening and lower toughness response compared to soft free slip (micro free) boundary conditions.
- The assessment of the effect of non-random orientation distribution (or texture effect) depends on the level of plastic strain developing in the specimen. Larger plastic strains result in smaller stress and traction values. For the specimen type used in this study and imposed boundary conditions, the failure tends to initiate at the grain boundaries that are close to the ends of the specimen. At later stages of loading, crack propagation interferes with the fixed ends of the specimen and this unfortunately masks the true response of the specimen. Therefore alternative specimen shapes and/or boundary conditions seem to be necessary to make a reliable assessment of non-randomness for relatively larger plastic strain distributions.
- The expected size effect is captured by the strain gradient crystal plasticity framework used here, for two different m values. The trend of higher strength and higher hardening slope gets clearly visible as the sample size is reduced. It is also to be noted that, for both relatively large plastic strains ($m = 0.2$) and low plastic strains ($m = 1$), the significant differences in peak stress values due to specimen size lead to local crack path changes.

The study requires further investigation, e.g. considering the size effect response. A detailed analysis with different number of grains would reveal the response of the framework in the context of both extrinsic and intrinsic size effect which is an interesting outlook for further studies. Moreover the influence of the length scale parameter should be investigated in detail which would have an impact on both the toughness of the material and fracture mode at the grain boundaries since the GND density evolution is highly affected by both size and the length scale parameter.

CRediT authorship contribution statement

T. Yalçinkaya: Conceptualization, Formal analysis, Investigation, Methodology, Resources, Software, Supervision, Validation, Visualization, Writing – original draft, Writing – review & editing. **İ.T. Tandoğan:** Formal analysis, Investigation, Validation, Visualization, Writing – original draft, Writing – review & editing. **İ. Özdemir:** Conceptualization, Formal analysis, Investigation, Methodology, Supervision, Validation, Visualization, Writing – original draft, Writing – review & editing.

Declaration of competing interest

The authors declare that they have no known competing financial interests or personal relationships that could have appeared to influence the work reported in this paper.

Acknowledgments

Tuncay Yalçinkaya gratefully acknowledges the support by the Scientific and Technological Research Council of Turkey (TÜBİTAK) under the 3501 Programme (Grant No. 117M106). Moreover the authors acknowledge the contributions of Prof. Alan Cocks from University of Oxford for the discussions in developing the cavity based cohesive zone relations.

Appendix. Supplementary information for derivation of traction-separation laws

For mode-I the evolution equation of f is derived using conservation of volume for incompressible matrix material, which results in $df = (dh/h)(1-f)$. For a change dh in height, the pore radius will grow by da, so conservation of volume reads,

$$\begin{aligned}
\pi(l^2-a^2)h &= \pi(l^2-(a+da)^2)(h+dh)\\
(l^2-a^2)h &= (l^2-a^2-2ada-da^2)(h+dh)\\
2ahda &= (l^2-a^2)dh \quad \text{where} \quad f = a^2/l^2\\
\frac{2ada}{l^2}h &= (1-f)dh \quad \text{where} \quad df = 2ada/l^2\\
hdf &= (1-f)dh.
\end{aligned}$$

Then it is assumed that when applied displacement δ_n is zero, $f = f_0$. And, when displacement is δ_n, pore fraction is f. Similarly, $h = h_0$ when $\delta_n = 0$, and it is h when displacement is δ_n. Then, if $df = (dh/h)(1-f)$ is integrated from $\delta_n = 0$ to δ_n,

$$\int_{f_0}^{f} \frac{1}{1-f}df = \int_{h_0}^{h} \frac{1}{h}dh$$

$$-ln(1-f)|_{f_0}^{f} = ln(h)|_{h_0}^{h}$$

$$ln\left(\frac{1-f_0}{1-f}\right) = ln\left(\frac{h}{h_0}\right).$$

Note that from mode-I boundary conditions $dh = d\delta_n$, therefore $h - h_0 = \delta_n - 0$. Or,

$$\frac{1-f_0}{1-f} = \frac{\delta_n + h_0}{h_0}.$$

By doing simple manipulations, f as a function of δ_n, initial pore fraction f_0 and initial pore height h_0 is obtained.

$$1-f = \frac{h_0(1-f_0)}{\delta_n + h_0}$$

$$f = \frac{\delta_n + h_0 f_0}{\delta_n + h_0}$$

Substituting $1-f$ and f to (14) results in (15). For mode-II a similar approach is followed. From the definition of pore fraction, $f = a^2/l^2$, it reads $df = 2\sqrt{f}(d\delta_t/l)$, where $da = d\delta_t$. Assume $f = f_0$ when $\delta_t = 0$ and take integral,

$$\begin{aligned}
\int_{f_0}^{f} \frac{df}{2\sqrt{f}} &= \int_0^{\delta_t} \frac{d\delta_t}{l}\\
\sqrt{f}|_{f_0}^{f} &= \frac{\delta_t}{l}|_0^{\delta_t}\\
f &= \left(\sqrt{f_0} + \frac{\delta_t}{l}\right)^2
\end{aligned}$$

Substituting f to (17) results in (18).

References

Alipour, A., Reese, S., Wulfinghoff, S., 2019. A grain boundary model for gradient-extended geometrically nonlinear crystal plasticity: Theory and numerics. Int. J. Plast. 118, 17–35.

van Beers, P., McShane, G., Kouznetsova, V., Geers, M., 2013. Grain boundary interface mechanics in strain gradient crystal plasticity. J. Mech. Phys. Solids 61 (12), 2659–2679.

Benallal, A., Billardon, R., Doghri, I., 1988. An integration algorithm and the corresponding consistent tangent operator for fully coupled elastoplastic and damage equations. Commun. Appl. Numer. Methods 4 (6), 731–740.

Benedetti, I., Aliabadi, M., 2013. A three-dimensional cohesive-frictional grain-boundary micromechanical model for intergranular degradation and failure in polycrystalline materials. Comput. Methods Appl. Mech. Engrg. 265, 36–62.

Benedetti, I., Gulizzi, V., Mallardo, V., 2016. A grain boundary formulation for crystal plasticity. Int. J. Plast. 83, 202–224.

Bond, D.M., Zikry, M.A., 2018. Differentiating between intergranular and transgranular fracture in polycrystalline aggregates. J. Mater. Sci. 53, 5786–5798.

Bronkhorst, C., Cho, H., Marcy, P., Vander Wiel, S., Gupta, S., Versino, D., Anghel, V., Gray, G., 2021. Local micro-mechanical stress conditions leading to pore nucleation during dynamic loading. Int. J. Plast. 137, 102903.

Cerrone, A., Wawrzynek, P., Nonn, A., Paulino, G.H., Ingraffea, A., 2014. Implementation and verification of the Park–Paulino–Roesler cohesive zone model in 3D. Eng. Fract. Mech. 120, 26–42.

Deschamps, A., Livet, F., BrYechet, Y., 1999. Influence of predeformation on ageing in an Al-Zn-Mg alloy.I. Microstructure evolution and mechanical properties. Acta Mater. 47, 281–292.

Dumont, D., Deschamps, A., Brechet, Y., 2003. On the relationship between microstructure, strength and toughness in AA7050 aluminum alloy. Mater. Sci. Eng. A 356 (1), 326–336.

Evers, L., Brekelmans, W., Geers, M., 2004. Non-local crystal plasticity model with intrinsic SSD and GND effects. J. Mech. Phys. Solids 52 (10), 2379–2401.

Fleck, N.A., Hutchinson, J.W., 1986. Void growth in shear. Proc. R. Soc. Lond. Ser. A Math. Phys. Eng. Sci. 407 (1833), 435–458.
Frodal, B.H., Thomesen, S., Børvik, T., Hopperstad, O.S., 2021. On the coupling of damage and single crystal plasticity for ductile polycrystalline materials. Int. J. Plast. 142, 102996.
Gurtin, M.E., 2002. A gradient theory of single-crystal viscoplasticity that accounts for geometrically necessary dislocations. J. Mech. Phys. Solids 50 (1), 5–32.
Gurtin, M.E., 2008. A theory of grain boundaries that accounts automatically for grain misorientation and grain-boundary orientation. J. Mech. Phys. Solids 56, 640–662.
Hardy, G., Littlewood, J.E., George, P., 1978. Inequalities. By G.H. Hardy, J.E. Littlewood, and G. Polya. Cambridge University Press.
Isfandbod, M., Martínez-Pañeda, E., 2021. A mechanism-based multi-trap phase field model for hydrogen assisted fracture. Int. J. Plast. 144, 103044.
Khadyko, M., Frodal, B.H., Hopperstad, O.S., 2021. Finite element simulation of ductile fracture in polycrystalline materials using a regularized porous crystal plasticity model. Int. J. Fract. 228, 15–31.
Klusemann, B., Yalcinkaya, T., 2013. Plastic deformation induced microstructure evolution through gradient enhanced crystal plasticity based on a non-convex Helmholtz energy. Int. J. Plast. 48, 168–188.
Klusemann, B., Yalcinkaya, T., Geers, M.G.D., Svendsen, B., 2013. Application of non-convex rate dependent gradient plasticity to the modeling and simulation of inelastic microstructure development and inhomogeneous material behavior. Comput. Mater. Sci. 80, 51–60.
Knight, S., Birbilis, N., Muddle, B., Trueman, A., Lynch, S., 2010. Correlations between intergranular stress corrosion cracking, grain-boundary microchemistry, and grain-boundary electrochemistry for Al–Zn–Mg–Cu alloys. Corros. Sci. 52 (12), 4073–4080.
Kuramoto, S., Itoh, G., Kanno, M., 1996. Intergranular fracture in some precipitation-hardened aluminum alloys at low temperatures. Metall. Mater. Trans. A 27, 3081–3088.
Kuroda, M., Tvergaard, V., 2006. Studies of scale dependent crystal viscoplasticity models. J. Mech. Phys. Solids 54 (9), 1789–1810.
Kuroda, M., Tvergaard, V., 2008. A finite deformation theory of higher-order gradient crystal plasticity. J. Mech. Phys. Solids 56 (8), 2573–2584.
Li, Y., Li, W., Min, N., Liu, H., Jin, X., 2020. Homogeneous elasto-plastic deformation and improved strain compatibility between austenite and ferrite in a co-precipitation hardened medium mn steel with enhanced hydrogen embrittlement resistance. Int. J. Plast. 133, 102805.
Liang, S., Huang, M., Zhao, L., Zhu, Y., Li, Z., 2021. Effect of multiple hydrogen embrittlement mechanisms on crack propagation behavior of FCC metals: Competition vs. synergy. Int. J. Plast. 143, 103023.
Liu, L.-Y., Yang, Q.-S., Liu, X., Nian, X.-C., 2021. Crystal cracking of grain-gradient aluminum by a combined CPFEM-CZM method. Eng. Fract. Mech. 242, 107507.
Ludtka, G.M., Laughlin, D.E., 1982. The influence of microstructure and strength on the fracture mode and toughness of "7XXX" series aluminum alloys. Metall. Trans. A. 13, 411–425.
Molkeri, A., Srivastava, A., Osovski, S., Needleman, A., 2019. Influence of grain size distribution on ductile intergranular crack growth resistance. J. Appl. Mech. 87, 031008.
Özdemir, İ., Yalçinkaya, T., 2014. Modeling of dislocation-grain boundary interactions in a strain gradient crystal plastictiy framework. Comput. Mech. 54, 255–268.
Özdemir, İ., Yalcinkaya, T., 2019. Strain gradient crystal plasticity: Intergranular microstructure formation.. Handbook of Nonlocal Continuum Mechanics for Materials and Structures. pp. 1035–1063.
Pardoen, T., Dumont, D., Deschamps, A., Brechet, Y., 2003. Grain boundary versus transgranular ductile failure. J. Mech. Phys. Solids 51 (4), 637–665.
Park, K., Paulino, G.H., Roesler, J.R., 2009. A unified potential-based cohesive model of mixed-mode fracture. J. Mech. Phys. Solids 57 (6), 891–908.
Quey, R., Dawson, P., Barbe, F., 2011. Large-scale 3D random polycrystals for the finite element method: Generation, meshing and remeshing. Comput. Methods Appl. Mech. Engrg. 200, 1729–1745.
Rao, A.U., Vasu, V., Govindaraju, M., Srinadh, K.S., 2016. Stress corrosion cracking behaviour of 7xxx aluminum alloys: A literature review. Trans. Nonferr. Met. Soc. China 26 (6), 1447–1471.
Rousselier, G., 2021. Porous plasticity revisited: Macroscopic and multiscale modeling. Int. J. Plast. 136, 102881.
Simonovski, I., Cizelj, L., 2015. Cohesive zone modeling of intergranular cracking in polycrystalline aggregates. Nucl. Eng. Des. 283, 139–147.
Singh, A., Pal, S., 2020. Coupled chemo-mechanical modeling of fracture in polycrystalline cathode for lithium-ion battery. Int. J. Plast. 127, 102636.
Tandoğan, I.T., 2020. Ductile fracture of metallic materials through micromechanics based cohesive zone elements (Master's thesis). Middle East Technical University.
Unwin, P., Lorimer, G.W., Nicholson, R., 1969. The origin of the grain boundary precipitate free zone. Acta Metall. 17, 1379–1393.
Vasudevan, A., Doherty, R., 1987. Grain boundary ductile fracture in precipitation hardened aluminum alloys. Acta Metall. 35 (6), 1193–1219.
Voyiadjis, G.Z., Song, Y., 2019. Strain gradient continuum plasticity theories: Theoretical, numerical and experimental investigations. Int. J. Plast. 121, 21–75.
Yalçinkaya, T., Brekelmans, W.A.M., Geers, M.G.D., 2012. Non-convex rate dependent strain gradient crystal plasticity and deformation patterning. Int. J. Solids Struct. 49, 2625–2636.
Yalçinkaya, T., Özdemir, İ., Simonovski, I., 2018. Micromechanical modeling of intrinsic and specimen size effects in microforming.. Int. J. Mater. Form. 11, 729–741.
Yalçinkaya, T., Özdemir, İ., Tandoğan, I.T., 2021. Misorientation and grain boundary orientation dependent grain boundary response in polycrystalline plasticity.. Comput. Mech. 67, 937–954.
Yalcinkaya, T., 2019. Strain gradient crystal plasticity: Thermodynamics and implementation. In: Handbook of Nonlocal Continuum Mechanics for Materials and Structures. pp. 1001–1033.
Yalçinkaya, T., Cocks, A., 2016. Micromechanical cohesive zone relations for ductile fracture. Procedia Struct. Integr. 2, 1716–1723.
Yalcinkaya, T., Özdemir, İ., Firat, A.O., 2019. Inter-granular cracking through strain gradient crystal plasticity and cohesive zone modeling approaches. Theor. Appl. Fract. Mech. 103, 102306.
Yalçinkaya, T., Tandogan, I.T., Cocks, A., 2019. Development of a micromechanics based cohesive zone model and application for ductile fracture. Procedia Struct. Integr. 21, 52–60.
Yefimov, S., Groma, I., Van der Giessen, E., 2004. A comparison of a statistical-mechanics based plasticity model with discrete dislocation plasticity calculations. J. Mech. Phys. Solids 52 (2), 279–300.